Article

High VEGF Secretion Using Co and B Co-doped Bioactive Mesoporous Glass Nanoparticles for Enhanced Angiogenesis

Martina Vitázková,* Fatih Kurtuldu, Nurshen Mutlu, Kai Zheng, Yan Xu, Pavol Šuly, Lukáš Münster, Zulema Vargas-Osorio, Dušan Galusek, and Martin Michálek*

Read Online

ACCESS | Metrics & More | Article Recommendations

ABSTRACT: This investigation presents a novel approach to engineering mesoporous bioactive glass nanoparticles (MBGNs) through selective ion doping. This method can significantly potentiate their physicochemical properties and biological performance. We elucidate the effects of boron (B) and cobalt (Co) doping, individually and in combination, on MBGNs' structural, functional, and biocompatible characteristics. Using microemulsion-assisted sol−gel synthesis, we fabricated MBGNs with sizes ranging from 150 to 250 nm and shapes that shifted from spherical to more irregular shapes upon co-doping, as observed by SEM and TEM. We assessed the materials' amorphous nature and molecular structure through XRD and FTIR, respectively, noting the preservation of bioactivity-associated Si−O−Si groups. This can influence the nucleation and growth of the mineral phases similar to those found in natural tissues, forming a bioactive coating on the material surface. Nitrogen adsorption−desorption isotherms confirmed a mesoporous structure with increased specific surface area upon co-doping. The release behavior of Ca and Si in simulated body fluids studied by ICP-OES indicated alterations after adding Co and B, modifying their release kinetics. Bone regeneration relies on osteogenesis and vascular network formation for nutrient and oxygen supply. This study highlights the synergistic effect of B and Co co-doping, enhancing both angiogenesis and osteogenesis beyond single-ion doping. Biocompatibility studies with MG-63 and HDFa cell lines indicated that B enhanced cell viability, while the viability effect of Co was concentration-dependent. Cytotoxicity was assessed through lactate dehydrogenase (LDH) assays and is shown in high concentrations in the case of reference and B-doped sample, which was significantly reduced in the case of co-doped material. The newly developed nanoparticles showed a 10-fold increase in vascular endothelial growth factor (VEGF) secretion compared to the control sample ($p < 0.05$, one-way ANOVA), as determined by enzyme-linked immunosorbent assay (ELISA) in treated cells. Based on present results, the co-doped system shows a strong potential impact on angiogenesis with no effect on cell cytotoxicity.
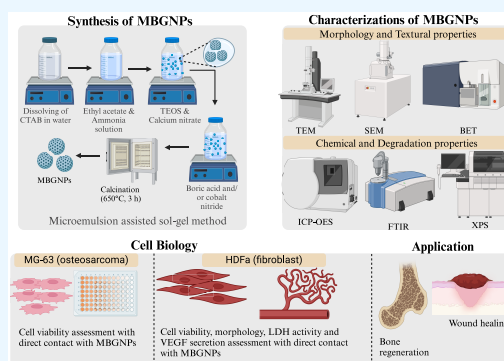
1. INTRODUCTION

Bioactive glass 45S5 (BG), developed by Hench et al. in 1969,[1] gained considerable attention as biomaterial due to its promising properties, such as bioactivity, osteoconductivity, and biodegradability.[2,3] Their great potential is mainly oriented toward tissue engineering and regenerative medicine applications. Recent progress has focused on enhancing the biological activity of BGs through the development of highly porous and nanosized materials.[4] Compared to traditional bioactive glasses, mesoporous bioactive glass nanoparticles (MBGNs) offer attractive advantages such as high specific surface area and mesoporous structure,[5] which makes them good candidates for drug delivery carriers.[6] For tissue engineering applications, doping MBGNs with therapeutic ions is a strategy to improve their functionality further.[7,8] These nanoparticles, tailored to deliver bioactive ions and growth factors, can provide antibacterial, pro-angiogenic, and osteogenic effects on tissue regeneration.[7,9] The incorporation of ions such as boron

and cobalt into bioactive glass scaffolds has shown promise for bone tissue engineering applications, promoting osteogenesis in human mesenchymal stem cells.[10−12]

Without adequate vascularization, engineered bone constructs face challenges such as limited nutrient diffusion, impaired cellular communication,[13,14] and compromised tissue integration, all of which can hinder the success of tissue repair and regeneration.[15,16] The importance of angiogenesis in wound healing and osteogenesis cannot be underestimated. In wound healing, angiogenesis is one of the earliest events initiated immediately after injury, serving to establish a
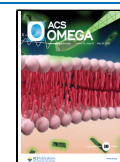
network of blood vessels that deliver oxygen and nutrients to the site of injury, remove metabolic waste products, and recruit immune cells to promote tissue repair.[17] Similarly, in bone regeneration, angiogenesis precedes osteogenesis, providing the necessary vascular network for bone precursor cells to migrate, proliferate, and differentiate into mature osteoblasts, which deposit a new bone matrix and facilitate tissue remodeling.

Recent studies have investigated the incorporation of various dopants into MBGNs to improve their biological properties.[7,8,18] For example, doping of cobalt or boron into MBGN has been investigated for its potential to enhance the angiogenic effect of these nanoparticles.[19] Bioactive glass fibers containing cobalt have been shown to stimulate the hypoxia-inducible factor-1 (HIF-1) pathway, which plays a key role in wound healing and angiogenesis.[11] In the case of mesoporous bioactive glass nanoparticles, the study was done by Zhang et al.[12] who incorporated the lithium and cobalt into the MBGN in a nominal concentration of 2 wt. %. In their work, they presented excellent pro-osteogenic differentiation ability in BMSC cell lines and pro-angiogenic ability in HUVECs cell lines. In addition, boron-doped bioactive silicate glasses demonstrated pro-angiogenic effects on endothelial cells, further highlighting the potential of dopants in enhancing angiogenesis.[20] In addition, developing novel delivery systems involving bioactive ions has shown promise in promoting angiogenesis and tissue regeneration.[21] While Co and B have demonstrated promising biological effects individually, their combined effects on MBGNs have not been comprehensively studied. Chen et al.,[19] in their study, prepared melt-quenched glass co-doped with cobalt and boron for enhanced pro-angiogenic properties and the most promising composition was based on 2 wt. % for both elements. The lack of data on their synergistic role in promoting angiogenesis and osteogenesis motivated this investigation within reactive materials, such as mesoporous bioactive glass nanoparticles.

Among all the possibilities, including ions, boron (B) and cobalt (Co) are of particular interest due to their roles in bone health and vascularization, respectively.[19,20] Boron, a trace element, has been implicated in bone development and maintenance in higher organisms.[22] Its role in cross-linking the extracellular matrix proteins and modulation of the inflammatory response underscores its potential in bone repair. When integrated into bioactive glasses, B can improve the mechanical properties and bioactivity, enhancing bone-forming capabilities. Moreover, B ions within the MBGNs increase metabolic activity and membrane stability.[20,23] Boron has also been reported to influence various other cellular processes, including cell signaling, gene expression, and metabolism, and play a role in the turnover and regulation of the extracellular matrix and increase the release of tumor necrosis factor alpha (TNF α).[22,24,25] The influence of cobalt on angiogenesis is well documented. However, it is important to note that different oxidation states of Co ions can lead to varying outcomes for the prepared material. The introduction of Co^{2+} and Co^{3+} ions can lead to complex interaction. The main criterion is determining the optimal concentration of introduced Co ions, as high concentrations can significantly reduce cell viability, proliferation, or ability to adhere to the surface. Co^{2+} ions are known precisely for their ability to mimic hypoxia by stabilizing the hypoxia-inducible factor (HIF), thus supporting cell survival despite low oxygen content. An important addition is that Co^{3+} ions exhibit different biochemical interactions than Co^{2+}.[26] The important difference is based on their redox activity and oxidative stress. Co^{2+} is less redox-active than Co^{3+} and can participate in Fenton-like reactions, which produces the reactive oxidative species (ROS), but typically not as much as Co^{3+}. Based on this, Co^{3+} can result in more pronounced cell damage and potentially lead to apoptosis.[27,28] Another important difference is in the binding of proteins and enzymes when Co^{2+} can replace other metal ions (e.g., Mg^{2+}, Zn^{2+}) in metalloproteins, which can cause potential alterations in their function.[29] Cobalt ions have also been shown to possess anti-inflammatory properties and may thus contribute to a more favorable healing process. In summary, Co stabilizes hypoxia-inducible factor-1 (HIF-1), upregulating VEGF expression and promoting endothelial cell proliferation,[12,30] while B supports osteoblast differentiation and extracellular matrix stability. Prior research on single-ion doping suggests potential synergy, which remains unexplored.

This study hypothesizes that co-doping mesoporous bioactive glass nanoparticles with boron and cobalt enhances vascular endothelial growth factor secretion and bioactivity compared to single-doped MBGNs. This research evaluates the structural and physicochemical properties of the materials through comprehensive characterization and *in vitro* testing, with a particular focus on their angiogenic potential. The study aims to enhance skeletal vascularization, wound healing, and bone defect repair by stimulating both angiogenic and osteogenic responses.

2. EXPERIMENTAL PROCEDURE

2.1. Materials. Tetraethyl orthosilicate (TEOS, $(C_2H_5O)_4Si$ 99%, Sigma-Aldrich), cetyltrimethylammonium bromide (CTAB, $CH_3(CH_2)_{15}N(Br)(CH_3)_3$, 99%, Sigma-Aldrich), ethyl acetate (EA, $CH_3COOC_2H_5$, Merck, Germany), ammonium hydroxide (NH_4OH ACS reagent, 28% NH_3 basis, Sigma-Aldrich), calcium nitrate tetrahydrate ($Ca(NO_3)_2\cdot4H_2O$, 99%, CentralChem, Slovakia), cobalt nitrate hexahydrate ($Co(NO_3)_2\cdot6H_2O$, p.a. $\geq$99%, CentralChem), and boric acid (H_3BO_3, p.a. $\geq$99,5%, CentralChem).

2.2. Synthesis of Co, B, and Co-doped MBGNs. MBGNs were synthesized using an adaptation of the microemulsion-assisted sol–gel method reported by Liang et al.[31] In this section, we briefly describe the procedure. First, 1.19 g of CTAB was added to 52 mL of Millipore water under magnetic stirring at 450 rpm until complete dissolution at 37 °C. Subsequently, the solution was cooled to 25 °C (reaction temperature was stabilized during the whole synthesis procedure), followed by adding 16 mL of ethyl acetate, and left for 30 min (stirred at 350 rpm throughout the following synthesis) before the incorporation of 1.74 mL of ammonium hydroxide under continuous stirring for another 15 min. After this time, 5.76 mL of TEOS and the calculated amount of the calcium nitrate tetrahydrate were added at 30 min intervals to prepare the reference binary material (REF) with a nominal composition of $60SiO_2-40CaO$ (mol %). For single-doped systems, reactions continue with the calculated amount of cobalt nitrate hexahydrate or boric acid, added 30 min after adding calcium nitrate. For the co-doped system, both cobalt and boron were added 30 min after the addition of the calcium nitrate tetrahydrate (see Table 1). Finally, the samples were calcinated for 3 h at a temperature of 650 °C with a heating rate of 1 °C/min.

2.3. Physicochemical Characterization of MBGNs. The chemical composition of the material was verified by

Table 1. Nominal Compositions of Mesoporous Bioactive Glass Nanoparticles (mol %)

MBGNs type	SiO_2	CaO	CoO	B_2O_3
REF	60	40		
3B	60	37		3
3Co	60	37	3	
3Co3B	60	34	3	3

inductively coupled plasma-optical emission spectroscopy (ICP-OES, Varian MPX) via an acid digestion method. Each sample was measured in three replicas. The measurements were done in radial plasma using 15 L/min Ar gas flow and radiofrequency power of 1.15 kW. The MBGNs were digested by microwave-assisted digestion (Speedwave 4, Berghof Products+Instruments, Germany) and prepared for analysis using a strong acid mixture prepared from 6 mL HCl, 0.5 mL HF, 2 mL HNO_3, and 5 mL of H_3PO_3. A series of at least three calibration solutions was prepared to obtain a linear correlation between the intensity of the ions and concentration. The calibration standards were prepared by appropriate dilution of the certified references (Analytika., s.r.o., Czech Republic) with 5% HNO_3 to enable at least a three-point calibration curve comprising a range from 5 to 100 mg/L for B, from 5 to 250 mg/L for Ca, from 3 to 165 mg/L for P, from 2.5 to 100 mg/L for Si, and from 2 to 100 ppm for Co. The internal standardization technique, with scandium as the internal standard, was used to deal with the nonspectral interferences. The precision of the analysis for all ions, expressed as RSD %, was below 5%. The average values, including standard deviations, were obtained from at least three replicates for each ion.

Scanning electron microscopy (SEM, JSM-7600 F, JEOL, Japan) and transmission electron microscopy (TEM, JEM-2100, JEOL, Japan) were used to examine the morphology and surface microstructure. The preparation of samples for SEM was as follows: MBGNs were dispersed in EtOH in a sonication bath for 1 min. Then, the suspension was dropped on the holder with carbon tape, followed by air drying. Samples were coated with platinum by using a Sputter-coater (Quorum Q150 V ES plus, U.K.) with a layer thickness of 10 nm. The shape of the synthesized nanoparticles was analyzed using ImageJ software (National Institutes of Health, Bethesda, MD), and at least 200 particles were used for each sample. The TEM analysis was performed at an accelerating voltage of 200 kV. The samples were dispersed in ethanol at 0.1 wt. % and ultrasonicated using an ultrasonic homogenizer WiseTis HG-15D (Witeg Labotechnik, Germany) for 30 s. Finally, the dispersed samples were dropped onto a copper grid (300 mesh) with a Formvar coating and dried at 40 °C.

X-ray diffraction analysis was performed using an X-ray diffractometer (Panalytical Empyrean DY1098, U.K.) with Cu Kα radiation (45 kV) in the 2Θ range of 20−80°. The surface of nanoparticles was characterized using X-ray photoelectron spectroscopy (XPS, Nexsa G2, Thermo-Scientific), equipped with monochromatic Al Kα radiation. A spot size of 400 μm was used for analysis. The survey spectra were acquired in the binding energy range of 0−1200 eV with an energy step size of 1 eV and a pass energy of 200 eV. High-resolution elemental XPS data were obtained using an energy step size of 0.1 eV and a pass energy of 50 eV. Fourier transform infrared spectroscopy (FTIR) analyses were done by using an FT-IR Spectrometer (Spectrum 3, PerkinElmer) in absorbance mode in the wavenumber range from 4000 to 400 cm^{-1} at a resolution of 4 cm^{-1}.

Nitrogen absorption/desorption isotherms were recorded with a volumetric gas adsorption analyzer (BELSORP Mini II, BEL Japan) at 77 K. Before measurements were taken, the samples were degassed in sample cells at 300 °C for 3 h. The specific surface area (SSA) was determined with multipoint Brunauer−Emmett−Teller (BET) analysis, applying at least five data points within a relative pressure range of 0.05−0.20 p/p_0 (Data Analysis Software, version 6.4.1.0, MicrotracBEL Corp., Japan).

2.4. _In Vitro_ Bioactivity. The material's ability to form hydroxyapatite was investigated using an _in vitro_ bioactivity assay. The bioactivity test was performed by immersing 75 mg of the material in 50 mL of simulated body fluid (SBF) according to Kokubo's method.[32] The bioactivity test was carried out at 37 °C under constant shaking at 120 rpm for 1, 3, 7, and 14 days. Samples were measured in triplicate. After each time point, supernatants were collected for ion release measurements. Subsequently, the supernatants were filtered using 0.22 μm syringe filters. Then, the samples were analyzed by optical emission spectroscopy with inductively coupled plasma (ICP-OES, Varian MPX). A series of at least three calibration solutions was prepared to obtain a linear correlation between the intensity of the signal and the concentration of measured ions. The reference standards certified for ICP techniques (Analytika spol., s.r.o., Czech Republic) were diluted to prepare the calibration solutions. The internal standardization technique, with scandium as the internal standard, was used to deal with nonspectral interferences. After the completion of bioactivity tests, the remaining powder samples were collected, washed with deionized water and acetone, and examined by using SEM, XRD, and FTIR.

2.5. Cell Culture. In this study, human osteoblast-like MG-63 and human primary fibroblast HDFa cell lines were used. MG-63 cells were cultured in Dulbecco's modified Eagle's media (DMEM, Gibco, Germany) supplemented with 10% Fetal Bovine Serum (FBS, Gibco, Germany) and 1% Penicillin−Streptomycin (PS, Gibco, Germany) at 37 °C in a humidified incubator with 5% CO_2. These cells were harvested using trypsin-EDTA (0.25%, Gibco, Germany) and resuspended in the cell culture medium as required. The HDFa cells were cultured in human fibroblast expansion basal medium (Gibco, Germany) supplemented with a low serum growth supplement (Gibco, Germany) under the same conditions as the MG-63 cells. HDFa cells were harvested using trypsin-EDTA (0.025%, Gibco, Germany). In this study, both cell lines were used for direct cytotoxicity assays. Additionally, fluorescence staining, VEGF-A release, and LDH release tests were performed by using HDFa cells.

Moreover, the ion release from nanoparticles was measured using ICP-OES in DMEM supplemented with 10% FBS and 1% PS to have a more realistic assessment of _in vitro_ conditions. One mg/mL concentration of nanoparticles was added to the cell culture medium and incubated at 37 °C under constant shaking at 120 rpm. After 48 h, supernatants were collected and filtrated with a 0.22 μm syringe filter. Then, samples were analyzed by ICP-OES, as mentioned in Section 2.3.

2.6. _In Vitro_ Cytotoxicity Assay. MG-63 and HDFa cell lines were seeded into 96-well plates with an inoculum ratio of 5×10^4 cells/mL in 3 replicates for each concentration and incubated at 37 °C in a humidified atmosphere of 5% CO_2 for
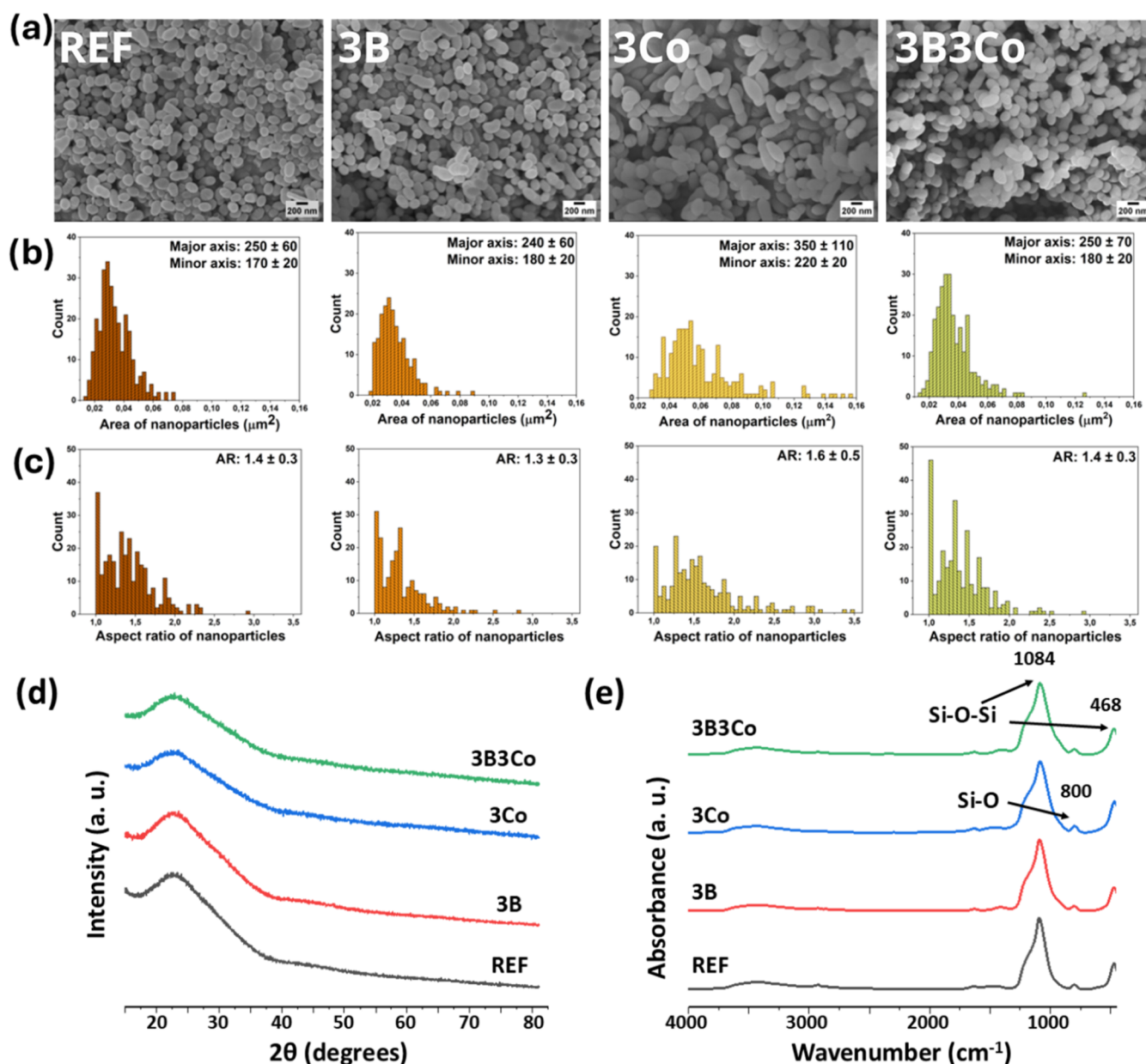
Figure 1. (a) SEM micrographs of MBGNs showing their morphology, (b) distribution of area of nanoparticles (μm^2) by count, (c) distribution of aspect ratio of nanoparticles (ratio of major and minor axis) by count—at least 200 nanoparticles analyzed for each sample, (d) X-ray diffraction (XRD) patterns of MBGNs showing the amorphous state in each sample, (e) Fourier transform infrared (FTIR) spectra between 400 and 4000 cm^{-1} wavenumbers of MBGNs.

24 h. MBGNs samples were disinfected for 1h under UV radiation. Using the respective cell culture media, MBGNs were dispersed in cell culture media at concentrations of 10, 50, 100, and 500 μg/mL. Then, the medium in the 96-well plates with cells was discarded and replaced with the cell culture media containing MBGNs. A cell culture medium without MBGNs was used as the control group. After 48 h, the cytotoxicity of both cell lines was measured by WST-8 assay (CCK-8 kit, Sigma-Aldrich, Germany). The cell culture medium containing 5% v/v WST-8 was added to cells and further incubated for 4 h. The solutions were transferred into a new 96-well plate to measure absorbance at 450 nm using a spectrometer microplate reader (BioTek Epoch). Relative cell viabilities were calculated as follows:

$$\text{cell viability } (\%) = \frac{\text{Abs. of sample} - \text{Abs. of blank}}{\text{Abs. of positive control} - \text{Abs. of blank}} \times 100$$

2.7. Fluorescent Microscopy Assay. Fluorescent staining was performed to observe the morphology of HDFa cells cultured in direct contact with MBGNs. After the WST-8 assay, the cells were washed with Dulbecco's phosphate-buffered saline (DPBS). The cells were then fixed with 4 wt. %/v formaldehyde in PBS solution for 15 min, and the well plate was washed with DPBS 3 times. F-actin staining was performed with 4 μL mL^{-1} of rhodamine phalloidin (R415, molecular probes, Thermo Fisher Scientific, Germany) for 30 min. Then, the cell nuclei were stained with 1 μL mL^{-1} DAPI (40,6-Diamidino-2-Phenylindole, Dihydrochloride, Thermo

Fisher Scientific, Germany) for 5 min. The well plate was then washed with DPBS. Finally, cell staining was evaluated using a fluorescence microscope (Eclipse Ts2R-FL, Nikon, Japan).

2.8. Measurement of VEGF-A Concentration and LDH Release. The HDFa cells were seeded before testing in the 5 × 10^{4} cells/mL density in 3 replicates for each concentration for both ELISA and also LDH study and incubated for 24 h. The secretion of VEGF-A from HDFa cells was detected using the Human VEGF-A ELISA kit (RayBiotech, Norcross). Medium from HDFa cells cultured in direct contact with nanoparticles was collected after cytotoxicity tests. The nanoparticles were separated from the medium using centrifugation, and these supernatants were used for the assay. The procedure followed the instructions provided by the manufacturer.

The lactate dehydrogenase (LDH) release in the HDFa cell culture media was also measured by using the LDH activity assay kit (MAK066, Sigma-Aldrich, Germany). 50 μL of cell culture medium was used to determine the LDH release. The procedure followed the manufacturer's instructions.

2.9. Statistical Analysis. Statistical analysis was conducted through one-way ANOVA and Bonferroni's test using the Origin 2018b software (OriginLab). Differences with a probability (P) value of less than 0.05 were considered to be statistically significant. The findings were presented as ± standard deviation (SD).

3. RESULTS

3.1. Physicochemical Characterization of MBGNs. The morphological characterization of the different MBGNs compositions was performed by SEM (Figure 1a). SEM micrographs show dispersed MBGNs with particle size variations ranging from 150 to 250 nm. The nanoparticles are characterized by either spherical or elongated pineal shapes. To evaluate the effects of different dopants on the shape and size of the nanoparticles, their sizes (expressed in terms of their areas) and aspect ratios were analyzed using ImageJ software (Figure 1b,c). The 3B and 3B3Co samples exhibited comparable area, major and minor axis diameters, and aspect ratios to the undoped REF sample. In contrast, the 3Co sample demonstrated a significant effect of Co doping on morphology compared with the other samples. The 3Co sample showed a wider range of nanoparticle area distribution, significantly higher major and minor axis diameters, and consequently, a higher aspect ratio (1.6 ± 0.5). To determine the composition of MBGNs, the samples were digested using a microwave-assisted acid digestion method, followed by ICP-OES measurement (Table 2). The nanoparticle's measured composition differs from the nominal composition (Table 1). Specifically, the results indicate a higher concentration of Co and B than the desired amount of 3 mol %. The concentration of Ca ions was significantly lower than the nominal composition: this phenomenon is well documented in the

Table 2. Actual Composition of MBGNs (mol %) Measured by ICP-OES. Each sample was measured in three replicas

MBGNs	SiO_2	CaO	CoO	B_2O_3
REF	83 ± 2	16.7 ± 0.2		
3B	80.6 ± 0.7	15.9 ± 0.1		3.56 ± 0.02
3Co	84 ± 2	11.7 ± 0.3	4.5 ± 0.1	
3B3Co	78.2 ± 0.2	13.2 ± 0.2	4.97 ± 0.07	3.39 ± 0.03

nanoparticles prepared by the microemulsion-assisted sol−gel technique.[4,33,34]

The XRD patterns measured in the 2θ range of 20−80° did not show any diffraction maxima corroborating that the synthesized nanoparticles were amorphous (Figure 1d). The chemical structure of the synthesized single-doped and co-doped materials was studied using FTIR spectroscopy (Figure 1e). The results show that structurally, the materials doped with either B or Co or both ions do not differ from the undoped nanoparticles. The nanoparticles showed characteristic FTIR spectra corresponding to sol−gel-based silicate glasses. An intense broadband at 1084 cm^{-1} and a less intense peak around 468 cm^{-1} are attributed to the stretching and rocking vibration modes of the Si−O−Si bonds, respectively.[35−38] The peak around 800 cm^{-1} is assigned to bridge bonds in SiO_4 tetrahedra.[35−38]

XPS analysis was carried out to confirm and provide further details on the oxidation state of the ionic species. Figure 2a shows the survey scan of XPS of MBGNs, while Figure 2b,c display high-resolution XPS spectra of B 1s and Co 2p, respectively. The survey scan confirms the presence of Si, Ca, B, and Co on the surfaces of the samples, which is consistent with the ICP-OES results. Furthermore, the high-resolution scan of the B 1s peak reveals a shift toward the lower energy side with the co-doped 3Co3B system. Chemical shift is associated with atoms in different bonding configurations.[39] It is worth noting that the low concentration of boron in the glass composition and overlapping Si 2s plasmon loss features make the interpretation of the B 1s spectra challenging.[40] Moreover, the high-resolution scan of Co 2p shows four peaks. The typical 2p peak pairs from spin−orbit splitting and shakeup satellite features were observed on the higher binding energy side. The 782 and 798 eV peaks correspond to Co 2p$_{3/2}$ and Co 2p$_{1/2}$, respectively.[30] Strong satellites recorded for single-doped and co-doped samples are attributed to the Co^{2+} species.[30] However, there is a change in the intensity of satellites between single-doped and co-doped samples. A decrease in the satellite intensity for the co-doped 3Co3B sample suggests the presence of Co^{3+}.[41] Moreover, the broader peak width for both samples indicates that cobalt is present in more than one oxidation state or coordination geometry.[41] As discussed in the introduction, the oxidation state of Co ions profoundly influences their biological and physiological function.

In summary, SEM analysis revealed that MBGNs ranged in size from 150 to 250 nm, exhibiting both spherical and elongated morphologies. Co doping significantly increased the nanoparticle size and aspect ratio. ICP-OES confirmed the incorporation of dopants, although actual concentrations of therapeutic ions slightly deviated from nominal values. XRD analysis verified the amorphous nature of the structure, while FTIR and XPS confirmed the chemical composition, indicating the presence of Co in multiple oxidation states.

To understand the internal arrangement and textural properties of synthesized MBGNs, TEM and N_2 adsorption−desorption analyses were performed (Figure 3). TEM micrographs showed the mesoporous structures of nanoparticles (Figure 3a), displaying heterogeneous structures with mostly slit-shaped pore morphologies for all compositions. The N_2 adsorption−desorption analysis results showed type IV isotherms with H4-type hysteresis loop in the case of the 3Co sample and H3-type hysteresis loops in the others, as shown in Figure 3b.[42] The H4-type hysteresis loop indicates wedge-
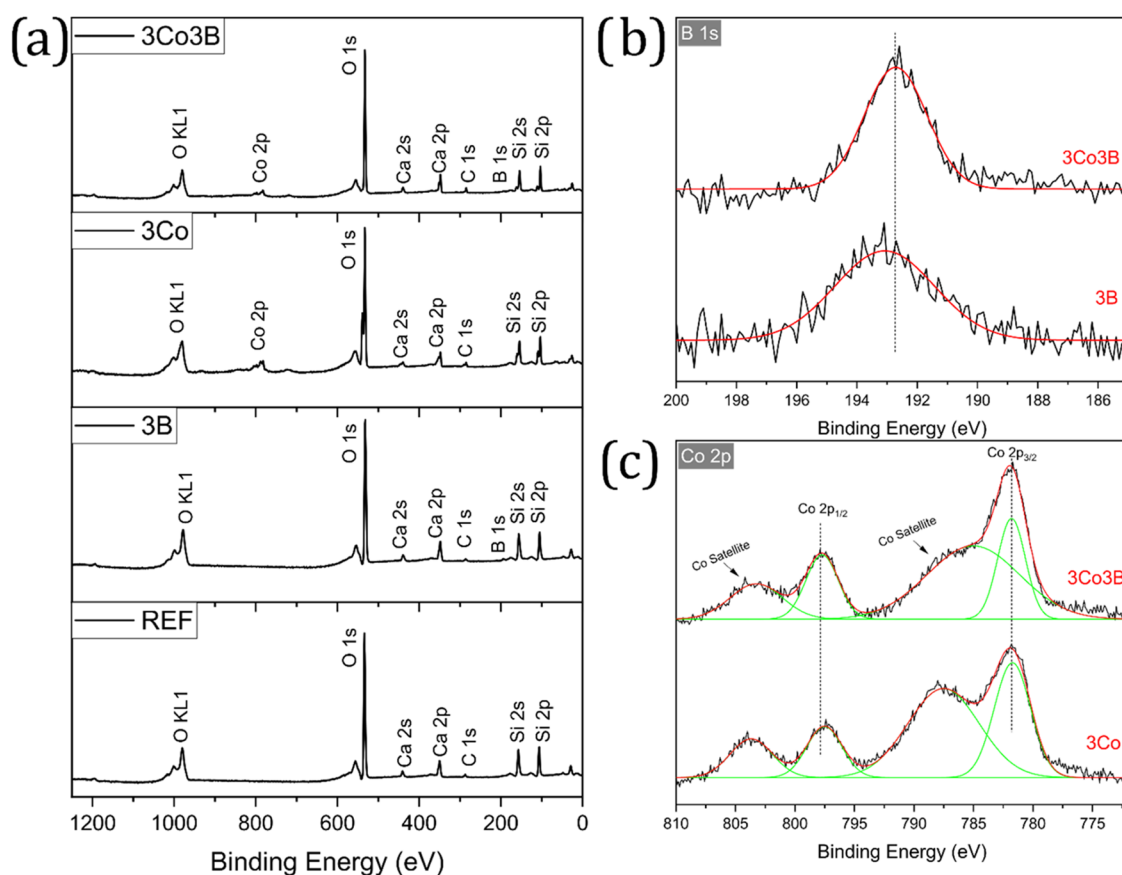
Figure 2. XPS spectra of mesoporous bioactive glass nanoparticles: (a) XPS survey scan, (b) high-resolution scan of B 1s, and (c) high-resolution scan of Co 2p.
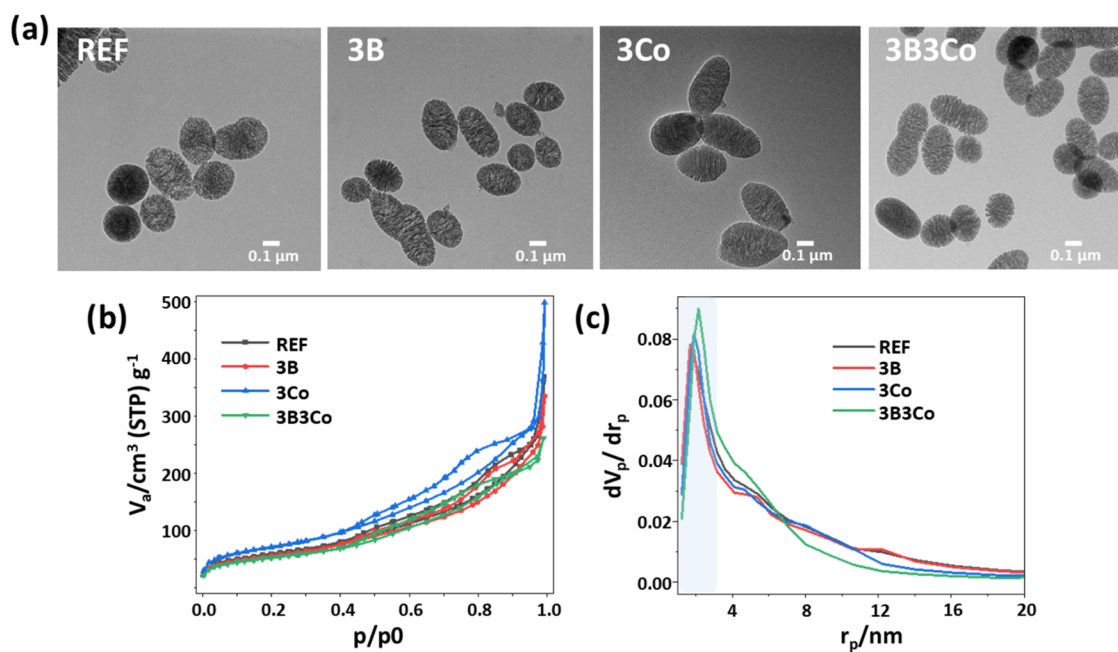

Figure 3. (a) TEM micrographs showing the morphology and porous structure of well-dispersed MBGNs, (b) Nitrogen adsorption isotherms of MBGNs, and (c) pore size distribution calculated from the adsorption isotherms based on the BJH method.

shaped pores, while H3-type hysteresis loops indicate that samples show slit-shape pores consistent with the TEM images.[42] The specific surface areas and total pore volumes of MBGNs are summarized in Table 3. REF and 3B samples showed similar specific surface areas. An increase in specific surface area and total pore volume was documented in the Co-doped MBGNs (3Co), the only ones that presented different pore shape. This result aligns with the image analysis of SEM

Table 3. Textural Properties and Particle Sizes of MBGNs[a]

type of MBGNs	S_{BET} (m^2/g)	V_p (cm^3/g)
REF	215	0.52
3B	202	0.46
3Co	260	0.59
3B3Co	190	0.40

[a]S_{BET}: Specific surface area; V_p: Total pore volume.

micrographs, which reveals a significantly larger size in the 3Co sample, while TEM micrographs do not indicate any reduction in the porosity. However, in the co-doped system, the presence of B decreased the specific surface area compared to the 3Co sample. This trend was consistent with the total pore volume results. Notably, 3Co exhibited the highest specific surface area (260 m^2/g) and total pore volume (0.59 cm^3/g).

SEM and TEM images confirm that B-doped MBGNs maintain a spherical morphology, whereas Co doping alters the particle shape to elongated structures. This is attributed to Co's effect on growth equilibrium during synthesis. TEM and N$_2$ adsorption–desorption confirmed mesoporosity, with Co doping increasing surface area and pore volume. Co-doped MBGNs (3Co) had wedge-shaped pores, while other samples exhibited slit-shaped pores. Co–B co-doping (3B3Co) also reduced porosity.

These findings confirm that the co-doping of MBGNs with boron and cobalt successfully modifies the physicochemical properties without disrupting the glass structure, supporting the objective of optimizing these materials for enhanced bioactivity and controlled ion release in biomedical applications.

3.1.1. In Vitro Bioactivity and Ion Release Behavior of MBGNs. Research on the bioactivity of MBGNs in simulated body fluid (SBF) provides crucial insights into their potential for biomedical applications. This analysis aimed to assess the suitability of MBGNs for applications in bone regeneration and tissue engineering, which are essential for addressing clinical challenges in orthopedics and regenerative medicine. Our analysis employed characterization techniques, including FTIR,

XRD, and SEM Figure 5 shows the XRD patterns and FTIR spectra of all MBGNs after 14 days of incubation. XRD pattern showed characteristic diffraction maxima of hydroxyapatite (HA)-like crystals in a possible semicrystalline phase (Figure 4b). The maxima observed at 2θ = 25.9 and 31.9°, respectively, correspond to the (002) and (211) planes of HA.[43] The XRD data have been cross-referenced with standard hydroxyapatite diffraction cards (JCPDS #09-0432), which confirm the presence of HA-like structures. The FTIR analysis complemented the XRD results in forming HA-like crystals (Figure 4c). In all compositions, the MBGNs systems showed promising signs of bioactivity demonstrated by the presence of a band between 900 and 1000 cm^{-1} associated with the stretching modes of the PO$_4^{3-}$ bonds in HA.[44,45] The band in the 565 and 606 cm^{-1} regions associated with the P–O bonding mode corresponds to the crystalline environment.

SEM micrographs (Figure 4a) provided visual confirmation of these findings and confirmed the presence of needle-like crystals placed between the nanoparticles and on their surfaces. The crystal phase formation and their nanocrystalline character are indicative of hydroxyapatite, suggesting its potential to promote mineralization and bone regeneration.[46] Similarities between single-doped and co-doped systems indicate that the biological behavior of these materials is not affected by the simultaneous presence of dopants.

The ion release results in Figure 5 were conducted in simulated body fluid (SBF) for 1, 3, 7, and 14 days. Silicon (Si) ion release remained relatively stable across all tested materials throughout the experimental period, with concentrations ranging from 32 ± 2 to 59.4 ± 0.5 mg/L. On the other hand, calcium (Ca) ion release exhibited notable differences between the Co-doped and reference materials, ranging from 60 ± 3 to 92 ± 4 mg/L for samples without boron and ranging from 66 ± 2 to 103 ± 2 mg/mL for boron-containing samples. Boron (B) ion release from the boron-doped (3B) and co-doped (3B3Co) materials did not show any significant differences in concentrations ranging from 7.5 ± 0.2 to 15.5 ± 0.6 mg/L throughout the experiment. The addition of B into
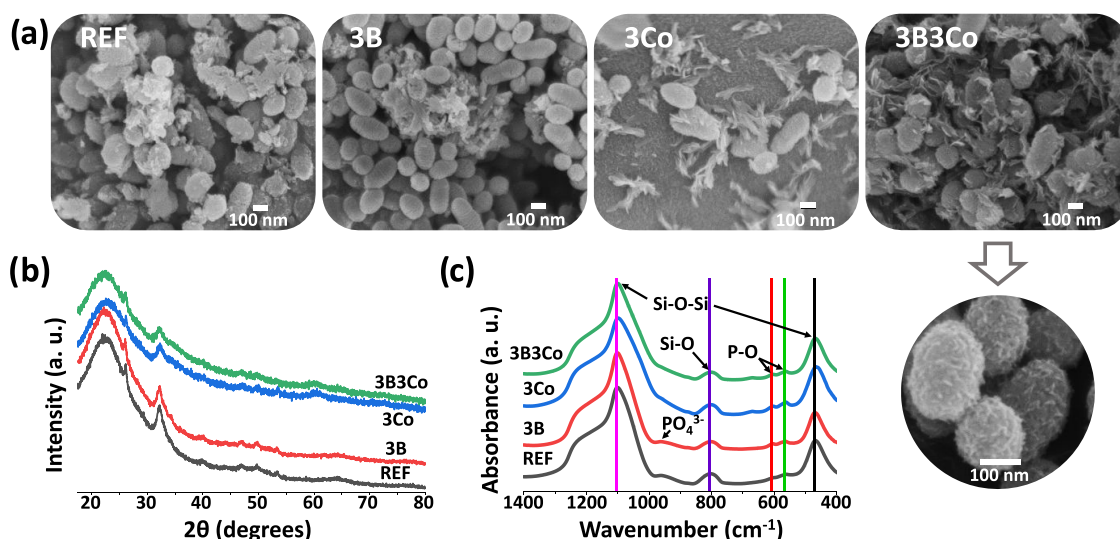

Figure 4. (a) SEM micrographs showing the creation of crystals dispersed between MBGNs and on their surface, which is shown in a representative magnified micrograph corresponding to a co-doped sample. (b) X-ray diffraction patterns (XRD) of MBGNs after immersion in SBF for 14 days measured in the 2θ range 10–80°. (c) FTIR spectra of MBGNs recorded between 400 and 1400 cm^{-1} after immersion in SBF for 14 days.
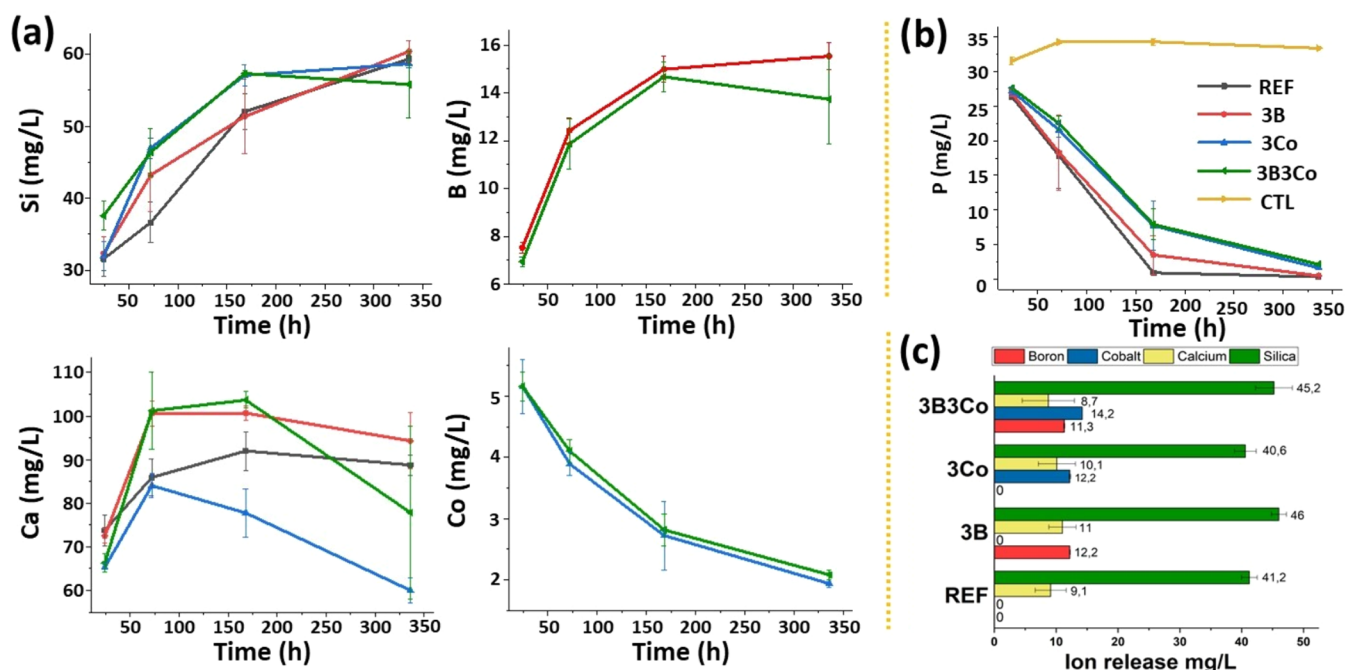
Figure 5. (a) Ion release profiles of MBGNs determined by ICP-OES in SBF for 1, 3, 7, and 14 days, measured in 3 replicas for each time point, (b) cumulative ion release profile of the P indicating the calcium phosphate crystallization from the media after calcium release, and (c) ion release from MBGNs after 48 h of soaking in complete DMEM cell culture media (mg/L).
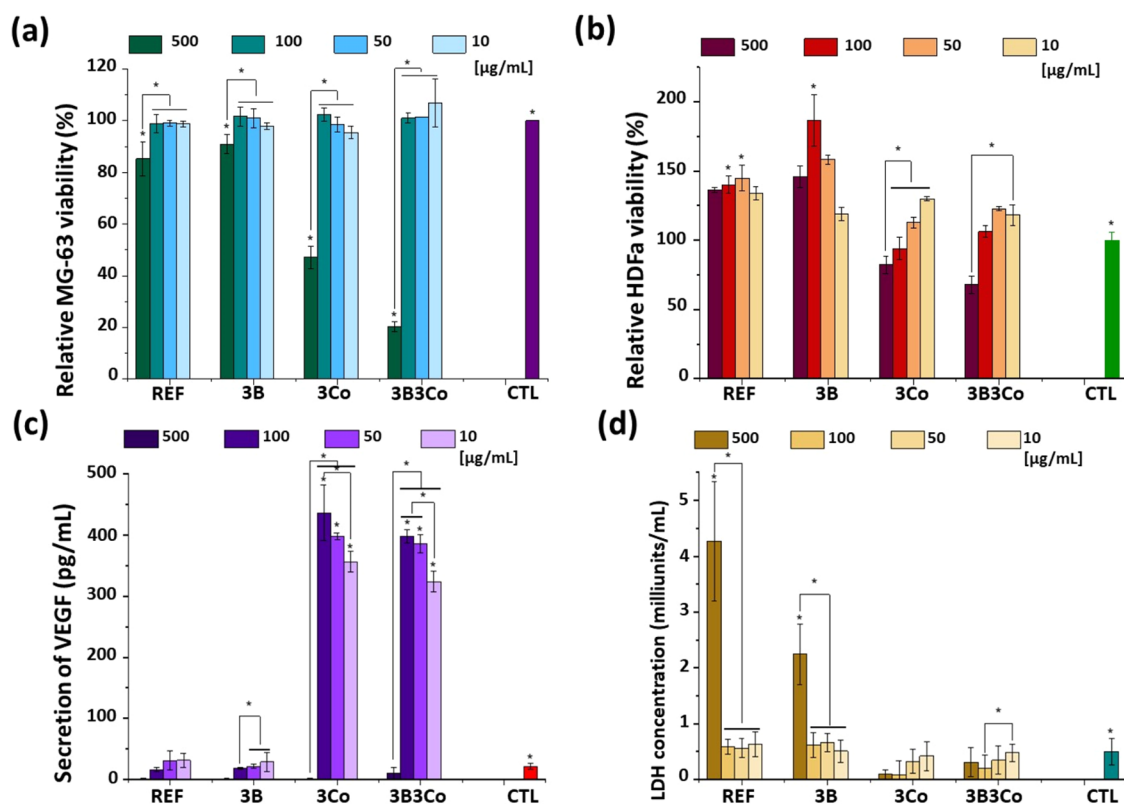

Figure 6. Relative viability (measured for 3 replicas in each concentration) of (a) MG-63 and (b) HDFa cells cultured in the presence of MBGNs other concentrations (500, 100, 50, and 10 μg/mL). (c) VEGF-A secretion from HDFa cells cultured for 48 h with MBGNs compared with control (CTL) and (d) LDH specific activity in cell culture medium after 48 h cultivation of MBGNs with the HDFa cell line. Statistical significances are indicated with *. The respective confidence intervals are $p < 0.05$ and were calculated via one-way ANOVA with Bonferroni correction.

the glass network in the case of 3B and 3B3Co increased the Ca release compared to that of REF. This can be explained by the presence of B in the glass structure, which disrupts the

silica network and accelerates glass dissolution. This assumption is further supported by the Si release from B-containing MBGNs, which was slightly higher than that from
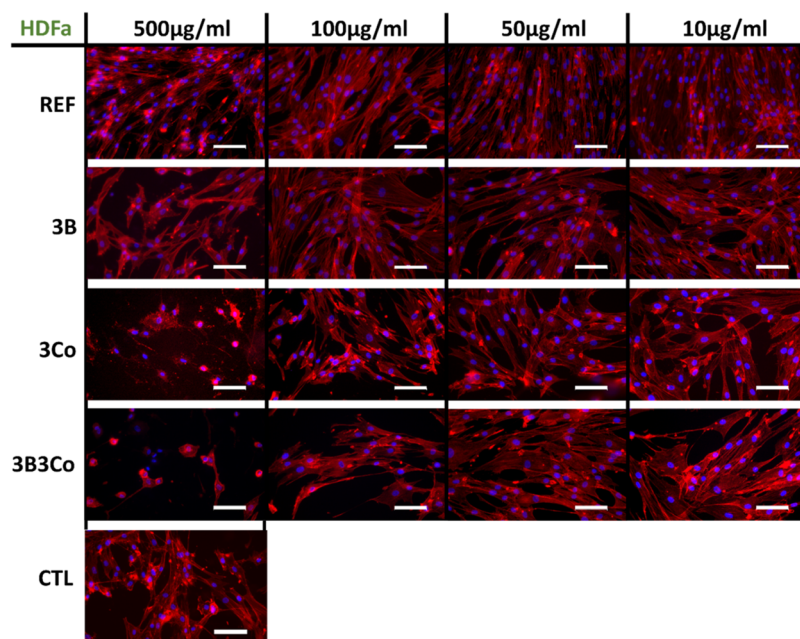
Figure 7. Evaluation of HDFa cell morphology after cell viability testing (stained with DAPI/Rhodamine phalloidin) by fluorescence microscope after cultivation with MBGNs in concentrations (500, 100, 50, and 10 μg/mL). Scale bars = 100 μm.

the REF sample. Cobalt (Co) ion release did not exhibit notable differences between the single-doped and co-doped, releasing between 2.7 ± 0.6 and 5.2 ± 0.4 mg/L. Phosphorus (P) ions were also monitored to assess the potential formation of HA-like structure. For all materials immersed in SBF, the P ions from the SBF medium showed a significant decrease compared to the blank sample (only SBF, denoted as CTL in Figure 5b). Therefore, this behavior could be attributed to HA-like phase formation in the SBF for all tested glasses. The formation of hydroxyapatite-like crystals in SBF and the controlled ion release profile validate the hypothesis that co-doped MBGNs maintain bioactivity while enhancing degradation properties. These results directly align with the study's goal of developing materials that can support both bone regeneration and angiogenesis.

In addition, the release of ions from MBGNs was analyzed in the complete cell medium (DMEM containing 10% FBS and 1% P/S) using the ICP-OES to verify whether the drop in the concentration of Co ions observed in the SBF would also occur in the cell medium. Ion release in a complete cell culture medium also provides insight for indirect *in vitro* biocompatibility assay. Figure 5c shows the amounts of ions released after immersion in DMEM for 48 h, corresponding to the time MBGNs were cultured with a cell culture medium. Boron ions released from boron-doped and co-doped materials range between 11.31 ± 0.07 and 12.21 ± 0.05 mg/L. The release of cobalt ions was particularly pronounced in the co-doped material and reached about 14.20 ± 0.01 mg/L. In contrast, in the singly doped material, the release of Co ions was about 12.2 ± 0.1 mg/L during the 48 h test period. The release of silicon ions remained relatively constant in all samples, averaging approximately 43 ± 3 mg/L. However, the content of released Ca ions shows significant differences compared to SBF media and ranges between 8 ± 2 and 11 ± 1 mg/L. The amount of P ions in the DMEM media also decreased from an average of 40 to 28−30 mg/L after 48 h of incubation with

MBGNs. The complete cell medium's ion release measurements showed quite different Co ion trends than in the SBF.

All MBGNs formed hydroxyapatite-like crystals in SBF, confirming the biological activity. Si ion release remained relatively stable, while Ca release increased in B-doped samples, indicating enhanced degradation. Co release was similar in single and co-doped samples, showing possible complexation in the SBF media, while in DMEM, it was not obtained this result. P decrease in SBF promoted HA formation. Direct comparison of ion release profiles in SBF versus DMEM highlights key differences. In SBF, a higher release of Ca and Si is observed, which promotes hydroxyapatite formation. In contrast, in DMEM, the medium contains many organic components with which these ions can interact, which alters their effect on the cytotoxicity. In DMEM, the presence of proteins and organic components also alters the bioavailability of Co, which affects the cytotoxicity and angiogenesis.

3.1.2. In Vitro Biocompatibility. Figure 6a shows the relative cell viability results of the MG-63 cell line cultured with MBGNs for 48 h at different concentrations of 10, 50, 100, and 500 μg/mL. The REF sample showed notable biocompatibility, exhibiting cell viabilities ranging from 85 ± 7 at 500 μg/mL to 99 ± 1 at 10 μg/mL. This suggests that REF is well-tolerated by MG-63 cells across the concentration spectrum. Interestingly, the 3B sample exhibited high cell viability, showing consistent values ranging from 90 ± 4 to 98 ± 1%. The boron incorporation into the MBGNs composition does not compromise biocompatibility and may even enhance it. Conversely, the 3Co sample displayed a concentration-dependent effect on cell viability. Cell viability decreased to 47 ± 4% at 500 μg/mL, indicating a potential cytotoxic effect. This observation requires further investigation into the underlying mechanisms of cytotoxicity associated with cobalt doping. Furthermore, the 3B3Co sample demonstrated variable viabilities across concentrations. At a concentration of 500 μg/mL, the cell viability was notably lower (20 ± 2%),

while at all other concentrations, the viability was similar or slightly higher than the control ($107 \pm 9\%$). This suggests a synergistic effect of boron and cobalt co-doping on biocompatibility, emphasizing the need for a detailed study of the mechanism involved.

Figure 6b shows the relative cell viability results of HDFa cell line cultured with MBGNs for 48 h at different concentrations of 10, 50, 100, and 500 μg/mL. The REF sample maintained excellent biocompatibility across all concentrations, with viabilities ranging from 136 ± 2 to $134 \pm 5\%$. This suggests that REF shows high compatibility with HDFa cells. In contrast, 3B displayed varying viabilities, ranging from 146 ± 8 to $119 \pm 5\%$ across concentrations. This variability may stem from the different cellular environments between MG-63 and HDFa cell lines, indicating the importance of cell-specific responses in biocompatibility evaluations. Furthermore, both 3Co and 3B3Co exhibited concentration-dependent effects on HDFa cell viability. While 3Co displayed viabilities ranging from 82 ± 6 to $130 \pm 2\%$, 3B3Co showed viabilities ranging from 68 ± 6 to $118 \pm 8\%$. These observations emphasize the need for a more profound comprehension and optimization of MBGN compositions tailored for specific biomedical applications.

Fluorescence microscopy was used to visualize the HDFa cell viability assay results, as shown in Figure 7. Accordingly, cells were stained with DAPI and Rhodamine Phalloidin according to a standardized procedure. This step allowed for visualization of the nuclei in the cells. Rhodamine Phalloidin staining was used to visualize the actin cytoskeleton by specific binding to filamentous actin, which produces a red fluorescent signal. No significant changes in cells' morphology and structural organization were demonstrated after exposure to MBGNs.

3.1.3. Measurement and Evaluation of VEGF-A and LDH Determination. The assessment of the vascular endothelial growth factor A (VEGF-A) concentration and lactate dehydrogenase (LDH) activity provides valuable insights into the angiogenic potential and cytotoxicity of mesoporous bioactive glass nanoparticles (MBGNs) (Figure 6c,d). Secreted VEGF-A from HDFa differs across varying concentrations (500, 100, 50, and 10 μg/mL). The reference sample (REF) gradually increased VEGF-A concentration, ranging from 16 ± 4 to 32 ± 11 pg/mL. Boron-doped MBGNs (B) displayed similar trends, with concentrations ranging from 18 ± 2 to 30 ± 20 pg/mL. Samples containing cobalt showed substantially higher VEGF-A concentrations, ranging from 360 ± 20 to 440 ± 50 pg/mL.

In LDH activity determination, REF demonstrated the highest LDH activity at the highest material concentration, with a significant decrease as concentrations decreased. Present results proved dosage-dependent biocompatibility and preserved membrane integrity. Boron-doped MBGNs (3B) displayed LDH activity levels comparable to those of REF, indicating the same dosage-dependent effects. Cobalt-doped MBGNs (3Co) demonstrated slight variations in LDH activity, suggesting minimal cytotoxicity and a high level of biocompatibility in each used concentration. The co-doped MBGNs (3B3Co) exhibited LDH activity similar to 3Co, indicating consistent biocompatibility. The control group showed LDH activity within the expected levels, indicating minimal cytotoxic effects under experimental conditions.

The comparison between the VEGF-A concentration and LDH activity provides valuable insights into the biocompat-

ibility and angiogenic potential of MBGNs. A direct comparison of VEGF-A secretion (Figure 6c) and LDH activity (Figure 6d) confirms the synergistic effect of B and Co co-doping. While B-doped MBGNs (3B) showed a minimal VEGF-A increase, Co-doped MBGNs (3Co) significantly enhanced secretion. The co-doped system (3B3Co) further amplified VEGF-A levels, suggesting that B ions enhance cell viability while Co drives angiogenesis. LDH activity was higher for 3B, indicating increased metabolism, while 3Co showed moderate levels. Notably, 3B3Co exhibited LDH activity lower than that of 3B, reducing B-related cytotoxicity.

The results collectively show that co-doping MBGNs with boron and cobalt enhances their structural, biological, and angiogenic properties. These findings align with the study's overarching objective of designing multifunctional bioactive glass nanoparticles that improve both osteogenesis and angiogenesis, addressing key challenges in tissue engineering.

4. DISCUSSION

Bone tissue formation, repair, and wound healing involve osteogenesis and angiogenesis. The main requirements for a biomaterial intended for these purposes are biodegradation, bioresorption, and activation of specific cells of interest.[47,48] Several studies have reported promising results.[11,12,19] Zhang et al.[12] prepared mesoporous bioactive glass nanoparticles by the sol−gel method with CTAB as a template agent in the system $SiO_2-CaO-P_2O_5$. Due to their promising pro-osteogenic and pro-angiogenic properties, the material was co-doped with lithium and cobalt. Their effects were verified on bone marrow stromal cells (BMSCs) and human umbilical vein endothelial cells (HUVECs), demonstrating their potential for bone tissue regeneration. Ege et al.[20] prepared mesoporous bioactive glass nanoparticles doped with boron ions in varying concentrations. They observed the effects of the differentiation of C2C12 cells (mouse myoblasts) into myotubes and evaluated the impact on muscle cell differentiation. Chen et al.[19] prepared multitargeted B and Co co-doped bioactive glass with 45S5 composition using a conventional melt quenching technique. The results demonstrated a significant increase in VEGF secretion in the bioactive glass containing 10 wt. % of B and 4 wt. % of Co, suggesting a potential impact on angiogenesis.

To investigate the synergistic effect of boron and cobalt co-doping, mesoporous bioactive glass nanoparticles, known for their inherent structural features, high specific surface area, and enhanced ion release, were synthesized using the micro-emulsion-assisted sol−gel method.[31,34] The addition of metallic ions during the synthesis affects the condensation process and shifts the growth equilibrium, disturbing the growth of nanoparticles and marking a progression from spherical to pineal shapes.[49]

The SEM images demonstrate that the incorporation of boron ions or both boron and cobalt ions into the structure only slightly alters the shape of the nanoparticles. Reference sample (REF) and samples containing boron (3B and 3B3Co) have particle sizes similar to the nanoparticles reported in previous studies.[12,33,50,51] Single cobalt doping (3Co) induces morphological changes in the nanoparticles compared with the other prepared materials, resulting in a higher aspect ratio (Figure 1c). Cobalt ions can affect the growth equilibrium during the formation of nanoparticles by inhibiting excessive particle aggregation. On the other hand, cobalt incorporation can enhance the stability of the mesoporous structure, which

prevents pore collapse during the calcination steps. These both can contribute to a higher specific surface area.[12,52]

As confirmed by ICP-OES analysis, the real chemical composition showed deviations from the nominal values, especially for the Ca and Si content, a well-known effect often reported for (60−40 mol %) SiO_2−CaO-based MBGNs prepared by the microemulsion-assisted sol−gel technique.[4,33,34] The concentration of Ca^{2+} ions was around 11.5−16.5 mol % and decreased with the addition of cobalt. This effect may be related to the replacement of CaO with dopant oxides, such as CoO, as part of the compositional adjustments.[52−54] The SiO_2 content was, in contrast, higher than expected. This discrepancy is likely attributed to variations in the reactivity and incorporation efficiency of the precursors during the sol−gel process. Notably, calcium nitrate is not initially incorporated into the sol−gel-derived glass network during the synthesis.[55] Instead, it is deposited onto the silica surfaces. During washing, some calcium nitrate is removed, leading to compositional differences. Thermal decomposition of calcium nitrate occurs between 500 and 600 °C. Consequently, the calcium nitrate decomposes during the calcination step at 650 °C into calcium oxide and subsequently incorporates into the sol−gel glass network as a modifier.[56] The higher Si and lower Ca ion content observed in this study are consistent with trends reported in the literature for similar mesoporous bioactive glass nanoparticles (MBGNs).[12,33,34,57] XPS measurements showed the presence of Co ions in the near-surface region of the silicate network, supporting their expected role as network modifiers that can ionically interact with nonbridging oxygen atoms. The oxidation state of cobalt ions may influence the ion release profile from MBGNs, as Co^{2+} tends to be released more readily than Co^{3+}, affecting the timing and extent of bioactivity and their therapeutic effects.[58]

According to Brauer et al.,[59] substituting Ca^{2+} for Co^{2+} obviously decreases Ca^{2+} content, which in turn causes a decrease in Ca^{2+} release and a delay in HA synthesis. However, the present study did not confirm any delay in hydroxyapatite (HA) formation, reported previously due to cobalt doping. This contradicts the findings of several other authors, mainly related to glass prepared by the conventional melt quenching method.[12,19,60,61] A significant release of the Co^{2+} ions was observed in this study in the first 24 h of immersion in SBF. A gradual color change in 3Co/3B3Co was also observed, from blue to pinkish during immersion in SBF (data not shown here), possibly indicating precipitation of cobalt complexes. A similar trend was observed by Solanki et al.,[62] who reported this effect by possible incorporation of cobalt in precipitated calcium phosphate. Therefore, the synthesized MBGNs underwent a 48 h ion release test in the DMEM medium to compare them with the SBF medium profile. Significant differences in Ca and reduced P ion concentrations were observed in SBF media, suggesting the possible formation of Ca−P-containing phases. Additionally, the DMEM, which contains potassium, calcium, amino acids, and other organic compounds, may also interact with Ca ions, indicating a need for extended ion release studies in various cell media.[63]

As a prerequisite for the successful application of a biomaterial in clinical practice, it must also pass biocompatibility tests. The evaluation methods are determined by the intended application, in our case, targeting angiogenesis enhancement. The most common mechanism for the internalization of nanoparticles into the cell is receptor-mediated endocytosis (RME) of various types, with clathrin or caveolin-mediated endocytosis being the most relevant.[64] However, the formation of vesicles coated with clathrin or caveolin proteins for subsequent internalization has a limit approximately in the range of 60−150 nm, and the influence of the shape of the nanoparticles on the extent of nanoparticle uptake by endocytosis is not precisely described.[64] Considering these insights, the dominant factor influencing biocompatibility in this study is assumed to be ion release from the dissolution of MBGNs rather than their internalization. Therefore, direct tests on MG-63 osteosarcoma-derived cells, commonly used to assess materials with potential osteogenic properties, and HDFa, human dermal fibroblasts, were conducted to provide insights into the material's effect on angiogenesis. The cell viability results for both cell lines showed no significant cytotoxic effect for the REF and 3B samples, even at the highest concentrations. In the case of HDFa cells, the viability increased significantly (by around 30%). These findings can confirm the importance of calcium and boron ions for cell signaling, proliferation, and apoptosis. The calcium ion is biology's most versatile and simplest second messenger.[65] Ca^{2+} represents one of the main ions in the extracellular matrix, which supports fibroblasts' structural integrity and function. Furthermore, Ca^{2+} significantly affects oxidative phosphorylation in mitochondria, which affects mitochondrial Ca^{2+} levels and leads to upregulation of citric acid cycle enzymes, resulting in increased ATP production and proliferation.[66−68]

After boron incorporation into the system, Ca^{2+} maintains cellular integrity and signaling, while B ions increase the metabolic activity and membrane stability. Although boron is not as intensively studied as calcium, it is known to play an important role in the stabilization of cell membranes and metabolic activity, promoting cell viability and proliferation.[20,23] Boron has also been reported to influence various other cellular processes, including cell signaling, gene expression, and metabolism, and play a role in the turnover and regulation of the extracellular matrix and augment the release of TNF α.[22,24,25] In line with previous studies on the effect of boron on mesenchymal stem cell proliferation and differentiation, our findings demonstrated that boron stimulated cell differentiation by significantly higher proliferation status.[69,70] The biocompatibility enhancing effect of boron-doped mesoporous bioactive glass nanoparticle extract in C2C12 cells by indirect viability test at concentrations of 1 mg/mL and lower during a 1-day incubation was demonstrated by Ege et al.[20] In our case, we directly tested our materials for 48 h with the cells and achieved good viability at every concentration with both undoped and boron-doped nanoparticles. The introduction of Co^{2+} and Co^{3+} ions together with Ca^{2+} also leads to a complex interaction. The main criterion is to find the correct concentration of introduced Co ions, as high concentrations can significantly reduce the viability of cells or significantly reduce their proliferation or ability to adhere to the surface. Co^{2+} ions are known precisely for their ability to mimic hypoxia by stabilizing hypoxia-inducible factor (HIF), thus supporting cell survival despite low oxygen content. An important addition is that Co^{3+} ions exhibit different biochemical interactions than Co^{2+}. However, Co^{3+} has been studied less regarding biological effectiveness due to its potential for higher toxicity by inducing oxidative stress and reduced cell viability and proliferation.[26] The important difference is based on their redox activity and oxidative stress. Co^{2+} is less redox-active than Co^{3+} and can

participate in Fenton-like reactions, which produces the reactive oxidative species (ROS), but typically not as much as Co^{3+}. Based on this, Co^{3+} can result in more pronounced cell damage and potentially lead to apoptosis.[27,28] Another important difference is in the binding of proteins and enzymes when Co^{2+} can replace other metal ions (e.g., Mg^{2+}, Zn^{2+}) in metalloproteins, which can cause potential alterations in their function.[29] The incorporation of Co^{2+} and Co^{3+} ions showed a significant viability decrease at the highest concentration for MG-63 cells, decreasing cell viability by approximately 20% in the case of the co-doped system. HDFa cells exhibited a moderate cytotoxic effect. A similar effect based on a dose-dependent manner was found in previous studies.[62,71] Lower concentrations of these materials did not show a decreased viability effect. In the case of the material co-doped with both B and Co, the decrease in viability at the highest concentration used was more moderate, probably due to the presence of B. Although a decrease in viability can still be observed, it is assumed that the boron ions will stabilize the cell membrane and promote metabolic processes, thus compensating for the co-induced cytotoxicity. Since the ion release kinetics are not the same for both ions, additional time intervals could be added to the tests to confirm the synergistic effect of the ions.

The cytotoxicity evaluation of HDFa cells in direct contact with MBGNs, based on LDH release, provided key insights into the cell membrane integrity and potential cytotoxic effects. Cobalt-containing MBGNs did not exhibit any cytotoxic effect, as indicated by the CCK-8 measurements. A higher LDH concentration in cell media collected after material testing with the cells was observed in the REF and 3B samples at the highest concentration (500 $\mu g/mL$). This result agrees with the reported effect of boron on the cell membrane, including cell signaling, gene expression, and metabolism.[20,23,72] Boron has been also shown to enhance cell proliferation significantly, although this is not necessarily directly associated with increased cell viability.[72,73] Conversely, cobalt ions might inhibit cell proliferation by upregulating hypoxia-inducible factors (HIFs), which are involved in regulating both apoptosis and angiogenesis.[74,75]

The effect of stimulation of VEGF-A expression by therapeutic ions on angiogenesis was tested by the ELISA method. As for REF and 3B materials, VEGF-A production was not enhanced compared with the control group. Significant differences were observed for the samples 3Co and 3B3Co: a 10-fold increase in VEGF-A production was detected, mainly at the second-highest concentration. This result agrees with previously reported data: Zhang et al.[12] used extracts of Co and Li-doped mesoporous bioactive glass nanoparticles to incubate HUVECs. They observed 6 times higher VEGF-A than those for the undoped glasses. The study of Chen et al.[19] showed a 2-fold VEGF-A expression for cobalt and boron-doped bioactive glass. In this case, a synergistic effect was achieved with the 45S5 glass fabricated using the conventional melting procedure. However, Chen et al. worked with the 24 h extracts of co-doped 45S5 and a concentration of 1 w/v%.

VEGF-A is a protein that plays a pivotal role in angiogenesis, the process by which new blood vessels form from existing ones.[76-78] Its significance arises from its multifaceted functions and extensive implications in various physiological and pathological processes. VEGF plays a vital role in ischemic diseases, neurogenesis, neuroprotection, diabetic retinopathy, macular degeneration, and tumor growth and metastasis.[79-82] Co doping mesoporous bioactive glass nanoparticles with B

and Co significantly boosted VEGF-A production without increasing LDH activity in HDFa cells, even at the highest concentration tested (Figure 6). Despite a decrease in viability and a noticeable slowdown in proliferation, the improved VEGF-A production highlights the potential of co-doped MBGNs. The material's synergy was confirmed when the presence of Co in the co-doped material significantly reduced LDH production compared to the material doped only with B. At the same time, viability in the two tested concentrations in HDFa cells was enhanced.

This study confirms the synergistic effects of boron and cobalt co-doping in MBGNs, enhancing bioactivity and angiogenesis. Structural analysis showed ion-induced morphological changes, while ion release studies highlighted their role in modulating bioactivity. Boron promoted cell proliferation, and cobalt significantly increased VEGF-A expression. Co doping mitigated cobalt-induced cytotoxicity, which supported its potential for regenerative applications. Further studies of ion release kinetics and gene expression are needed. These findings provide an opportunity for further biocompatibility tests for various concentrations of applied material at different time intervals. The focus will be on the gene expression of both pro-angiogenic and pro-osteogenic genes. Based on the verified release profile in the SBF medium, it is possible to predict the material's cascading effect on gene expression, as their burst release does not occur simultaneously. However, it is important to include an ion release study for the cell culture medium not just in one time point but for each in which the biocompatibility study will be done during the follow-up testing. This requires a much more complex and extensive biological study.

5. CONCLUSIONS

The present study successfully synthesized mesoporous bioactive glass nanoparticles (MBGNs) co-doped with cobalt (Co) and boron (B) using a microemulsion-assisted sol−gel method. The results demonstrated that co-doping with Co and B ions significantly enhanced the material's bioactivity and angiogenic potential, achieving up to a 10-fold increase in vascular endothelial growth factor (VEGF) secretion. This indicates that the controlled release of Co and B ions plays a crucial role in promoting angiogenesis while maintaining the biocompatibility. Furthermore, the material's ability to form hydroxyapatite-like crystals underscores its potential for applications in tissue engineering and regenerative medicine. Specifically, these MBGNs show promise for use as bone fillers or scaffolds designed to support vascularized skeletal formation. However, some limitations remain. The kinetics of ion release in diverse biological environments requires further investigation to optimize therapeutic effects and minimize potential cytotoxicity. Future research should focus on fine-tuning ion doping strategies to achieve controlled angiogenesis, while expanding studies to include multiple cell models and evaluating osteogenic properties. Additionally, exploring composite materials incorporating these MBGNs and conducting *in vivo* testing will be essential for advancing their clinical potential.

■ AUTHOR INFORMATION

Corresponding Authors

Martina Vitázková − FunGlass, A. Dubček University of Trenčín, 911 50 Trenčín, Slovakia; ● orcid.org/0009-0009-3775-8994; Email: martina.vitazkova@tnuni.sk

Martin Michálek − *FunGlass, A. Dubček University of Trenčín, 911 50 Trenčín, Slovakia;* Email: martin.michalek@tnuni.sk

Authors

Fatih Kurtuldu − *FunGlass, A. Dubček University of Trenčín, 911 50 Trenčín, Slovakia;* orcid.org/0000-0003-1344-8851

Nurshen Mutlu − *FunGlass, A. Dubček University of Trenčín, 911 50 Trenčín, Slovakia;* Present Address: Empa, Swiss Federal Laboratories for Materials Science and Technology, Technology and Society Laboratory, 9014 St. Gallen, Switzerland

Kai Zheng − *Jiangsu Province Engineering Research Center of Stomatological Translational Medicine, Nanjing Medical University, Nanjing 210029, China*

Yan Xu − *Jiangsu Province Engineering Research Center of Stomatological Translational Medicine, Nanjing Medical University, Nanjing 210029, China*

Pavol Šuly − *Centre of Polymer Systems, Tomas Bata University in Zlín, 760 01 Zlín 1, Czech Republic;* orcid.org/0000-0002-7500-7800

Lukáš Münster − *Centre of Polymer Systems, Tomas Bata University in Zlín, 760 01 Zlín 1, Czech Republic;* orcid.org/0000-0003-1643-2038

Zulema Vargas-Osorio − *FunGlass, A. Dubček University of Trenčín, 911 50 Trenčín, Slovakia*

Dušan Galusek − *FunGlass, A. Dubček University of Trenčín, 911 50 Trenčín, Slovakia; VILA − Joint Glass Centre of the IIC SAS, TnUAD, FChPT STU, 911 50 Trenčín, Slovakia*

Complete contact information is available at:
https://pubs.acs.org/10.1021/acsomega.5c00874

Author Contributions

M.V.: Conceptualization, validation, investigation, data curation, writing—original draft, visualization. F.K.: Validation, investigation, data curation, writing—review & editing. N.M.: Validation, investigation, data curation, writing—review & editing. K.Z.: Writing—review & editing resources. Y.X.: Writing—review & editing resources. P.S.: Data curation, investigation. L.M.: Data curation, investigation. Z.V.-O.: Data curation, writing—review & editing. D.G.: Resources, writing—review & editing. M.M.: Resources, validation, writing—review & editing.

Notes

The authors declare no competing financial interest.

REFERENCES

(1) Hench, L. L.; Splinter, R. J.; Allen, W. C.; Greenlee, T. K. Bonding Mechanisms at the Interface of Ceramic Prosthetic Materials. *J. Biomed. Mater. Res.* **1971**, *5* (6), 117−141.

(2) Hench, L. L.; Thompson, I. Twenty-First Century Challenges for Biomaterials. *J. R. Soc. Interface* **2010**, *7*, No. e1, DOI: 10.1098/rsif.2010.0151.focus.

(3) Jones, J. R. Review of Bioactive Glass: From Hench to Hybrids. *Acta Biomater.* **2013**, *9* (1), 4457−4486.

(4) Zheng, K.; Boccaccini, A. R. Sol-Gel Processing of Bioactive Glass Nanoparticles: A Review. *Adv. Colloid Interface Sci.* **2017**, *249*, 363−373.

(5) Manzano, M.; Vallet-Regí, M. Mesoporous Silica Nanoparticles in Nanomedicine Applications. *J. Mater. Sci. Mater. Med.* **2018**, *29* (5), No. 65, DOI: 10.1007/s10856-018-6069-x.

(6) Vallet-Regí, M.; Balas, F.; Arcos, D. Mesoporous Materials for Drug Delivery. *Angew. Chem., Int. Ed.* **2007**, *46* (40), 7548−7558.

(7) Zhu, H.; Zheng, K.; Boccaccini, A. R. Multi-Functional Silica-Based Mesoporous Materials for Simultaneous Delivery of Biologically Active Ions and Therapeutic Biomolecules. *Acta Biomater.* **2021**, *129*, 1−17.

(8) Kaya, S.; Cresswell, M.; Boccaccini, A. R. Mesoporous Silica-Based Bioactive Glasses for Antibiotic-Free Antibacterial Applications. *Mater. Sci. Eng. C* **2018**, *83*, 99−107.

(9) El-Fiqi, A.; Mandakhbayar, N.; Jo, S.; Knowles, J. C.; Lee, J. H.; Kim, H. W. Nanotherapeutics for Regeneration of Degenerated Tissue Infected by Bacteria through the Multiple Delivery of Bioactive Ions and Growth Factor with Antibacterial/Angiogenic and Osteogenic/Odontogenic Capacity. *Bioact. Mater.* **2021**, *6* (1), 123−136.

(10) Pinto e Souza, I. E.; Barrioni, B. R.; Miriceia, N. M. L.; Sachs, D.; Ribeiro, G. C.; Soares, D. C. F.; Pereira, M. M.; Nunes, E. H. M. Synergistic Effect of Cobalt and Cerium on the Structural Properties and Biological Behavior of Sol-Gel-Derived Mesoporous Bioactive Glass Nanoparticles. *J. Non-Cryst. Solids* **2023**, *613*, 122391.

(11) Solanki, A. K.; Autefage, H.; Rodriguez, A. R.; Agarwal, S.; Penide, J.; Mahat, M.; Whittaker, T.; Nommeots-Nomm, A.; Littmann, E.; Payne, D. J.; Metcalfe, A. D.; Quintero, F.; Pou, J.; Stevens, M. M.; Jones, J. R. Cobalt Containing Glass Fibres and Their Synergistic Effect on the HIF-1 Pathway for Wound Healing Applications. *Front. Bioeng. Biotechnol.* **2023**, *11*, 1125060.

(12) Zhang, X.; Nan, K.; Zhang, Y.; Song, K.; Geng, Z.; Shang, D.; Fan, L. Lithium and Cobalt Co-Doped Mesoporous Bioactive Glass Nanoparticles Promote Osteogenesis and Angiogenesis in Bone Regeneration. *Front. Bioeng. Biotechnol.* **2023**, *11*, 1288393.

(13) Hankenson, K. D.; Dishowitz, M.; Gray, C.; Schenker, M. Angiogenesis in Bone Regeneration. *Injury* **2011**, *42* (6), 556−561.

(14) Augustine, R.; Prasad, P.; Khalaf, I. M. N. Therapeutic Angiogenesis: From Conventional Approaches to Recent Nanotechnology-Based Interventions. *Mater. Sci. Eng. C* **2019**, *97*, 994−1008.

(15) Amini, A. R.; Laurencin, C. T.; Nukavarapu, S. P. Bone Tissue Engineering: Recent Advances and Challenges. *Crit. Rev. Biomed. Eng.* **2012**, *40* (5), 363−408.

(16) Schott, N. G.; Friend, N. E.; Stegemann, J. P. Coupling Osteogenesis and Vasculogenesis in Engineered Orthopedic Tissues. *Tissue Eng., Part B* **2021**, *27* (3), 199−214.

(17) Veith, A. P.; Henderson, K.; Spencer, A.; Sligar, A. D.; Baker, A. B. Therapeutic Strategies for Enhancing Angiogenesis in Wound Healing. *Adv. Drug Delivery Rev.* **2019**, *146*, 97−125.

(18) Pantulap, U.; Arango-Ospina, M.; Boccaccini, A. R. Bioactive Glasses Incorporating Less-Common Ions to Improve Biological and Physical Properties. *J. Mater. Sci. Mater. Med.* **2022**, *33* (1), No. 3, DOI: 10.1007/s10856-021-06626-3.

(19) Chen, S.; Michálek, M.; Galusková, D.; Michálková, M.; Švančárek, P.; Talimian, A.; Kaňková, H.; Kraxner, J.; Zheng, K.; Liverani, L.; Galusek, D.; Boccaccini, A. R. Multi-Targeted B and Co Co-Doped 45S5 Bioactive Glasses with Angiogenic Potential for Bone Regeneration. *Mater. Sci. Eng. C* **2020**, *112*, No. 110909.

(20) Ege, D.; Nawaz, Q.; Beltrán, A. M.; Boccaccini, A. R. Effect of Boron-Doped Mesoporous Bioactive Glass Nanoparticles on C2C12 Cell Viability and Differentiation: Potential for Muscle Tissue Application. *ACS Biomater. Sci. Eng.* **2022**, *8* (12), 5273−5283.

(21) Bromet, B. A.; Blackwell, N. P.; Abokefa, N.; Freudenberger, P.; Blatt, R. L.; Brow, R. K.; Semon, J. A. The Angiogenic Potential of PH-Neutral Borophosphate Bioactive Glasses. *J. Biomed. Mater. Res., Part A* **2023**, *111* (10), 1554−1564.

(22) Pizzorno, L. Nothing Boring about Boron. *Integr. Med.* **2015**, *14* (4), 35−48.

(23) Ege, D.; Zheng, K.; Boccaccini, A. R. Borate Bioactive Glasses (BBG): Bone Regeneration, Wound Healing Applications, and Future Directions. *ACS Appl. Bio Mater.* **2022**, *5* (8), 3608−3622.

(24) Şahin, F.; Pirouzpanah, M. B.; Farshbaf-Khalili, A.; Ayşan, E.; Doğan, A.; Demirci, S.; Ostadrahimi, A.; Mobasseri, M. The Effect of the Boron-Based Gel on the Treatment of Diabetic Foot Ulcers: A Prospective, Randomized Controlled Trial. *J. Trace Elem. Med. Biol.* **2023**, *79*, 127261.

(25) Paties Montagner, G.; Dominici, S.; Piaggi, S.; Pompella, A.; Corti, A. Redox Mechanisms Underlying the Cytostatic Effects of Boric Acid on Cancer Cells—An Issue Still Open. *Antioxidants* **2023**, *12* (6), No. 1302.

(26) Cárdenas-Triviño, G.; Elgueta, C.; Vergara, L.; Ojeda, J.; Valenzuela, A.; Cruzat, C. Chitosan Doped with Nanoparticles of Copper, Nickel and Cobalt. *Int. J. Biol. Macromol.* **2017**, *104*, 498−507.

(27) Simonsen, L. O.; Harbak, H.; Bennekou, P. Cobalt Metabolism and Toxicology-A Brief Update. *Sci. Total Environ.* **2012**, *432*, 210−215.

(28) Valko, M.; Morris, H.; Cronin, M. Metals, Toxicity and Oxidative Stress. *Curr. Med. Chem.* **2005**, *12* (10), 1161−1208.

(29) Sellin, S.; Mannervik, B. Metal Dissociation Constants for Glyoxylase I Reconstituted with Zn^{2+}, Co^{2+}, Mn^{2+}, and Mg^{2+}. *J. Biol. Chem.* **1984**, *259* (18), 11426−11429.

(30) Barrioni, B. R.; Norris, E.; Jones, J. R.; Pereira, M. M. The Influence of Cobalt Incorporation and Cobalt Precursor Selection on the Structure and Bioactivity of Sol−gel-Derived Bioactive Glass. *J. Sol−Gel Sci. Technol.* **2018**, *88* (2), 309−321.

(31) Liang, Q.; Hu, Q.; Miao, G.; Yuan, B.; Chen, X. A Facile Synthesis of Novel Mesoporous Bioactive Glass Nanoparticles with Various Morphologies and Tunable Mesostructure by Sacrificial Liquid Template Method. *Mater. Lett.* **2015**, *148*, 45−49.

(32) Maçon, A. L. B.; Kim, T. B.; Valliant, E. M.; Goetschius, K.; Brow, R. K.; Day, D. E.; Hoppe, A.; Boccaccini, A. R.; Kim, I. Y.; Ohtsuki, C.; Kokubo, T.; Osaka, A.; Vallet-Regí, M.; Arcos, D.; Fraile, L.; Salinas, A. J.; Teixeira, A. V.; Vueva, Y.; Almeida, R. M.; Miola, M.; Vitale-Brovarone, C.; Verné, E.; Höland, W.; Jones, J. R. A Unified in Vitro Evaluation for Apatite-Forming Ability of Bioactive Glasses and Their Variants. *J. Mater. Sci. Mater. Med.* **2015**, *26* (2), 115.

(33) Kurtuldu, F.; Mutlu, N.; Michálek, M.; Zheng, K.; Masar, M.; Liverani, L.; Chen, S.; Galusek, D.; Boccaccini, A. R. Cerium and Gallium Containing Mesoporous Bioactive Glass Nanoparticles for Bone Regeneration: Bioactivity, Biocompatibility and Antibacterial Activity. *Mater. Sci. Eng. C* **2021**, *124*, 112050.

(34) Neščáková, Z.; Zheng, K.; Liverani, L.; Nawaz, Q.; Galusková, D.; Kaňková, H.; Michálek, M.; Galusek, D.; Boccaccini, A. R. Multifunctional Zinc Ion Doped Sol − Gel Derived Mesoporous Bioactive Glass Nanoparticles for Biomedical Applications. *Bioact. Mater.* **2019**, *4*, 312−321.

(35) Serra, J.; González, P.; Liste, S.; Serra, C.; Chiussi, S.; León, B.; Pérez-Amor, M.; Ylänen, H. O.; Hupa, M. FTIR and XPS Studies of Bioactive Silica Based Glasses. *J. Non-Cryst. Solids* **2003**, *332* (1−3), 20−27.

(36) Filgueiras, M. R. T.; La Torre, G.; Hench, L. L. Solution Effects on the Surface Reactions of Three Bioactive Glass Compositions. *J. Biomed. Mater. Res.* **1993**, *27* (12), 1485−1493.

(37) Aguiar, H.; González, P.; Serra, J. *Bioactive Glass Structure and Solubility*, 2nd ed.; Elsevier Ltd., 2018.

(38) Christie, J. K.; Ainsworth, R. I.; De Leeuw, N. H. Investigating Structural Features Which Control the Dissolution of Bioactive Phosphate Glasses: Beyond the Network Connectivity. *J. Non-Cryst. Solids* **2016**, *432*, 31−34.

(39) Miura, Y.; Kusano, H.; Nanba, T.; Matsumoto, S. X-Ray Photoelectron Spectroscopy of Sodium Borosilicate Glasses. *J. Non-Cryst. Solids* **2001**, *290* (1), 1−14.

(40) Caussat, B.; Scheid, E.; de Mauduit, B.; Berjoan, R. Influence of Dopant Concentration and Type of Substrate on the Local Organization of Low-Pressure Chemical Vapour Deposition in Situ Boron Doped Silicon Films from Silane and Boron Trichloride. *Thin Solid Films* **2004**, *446* (2), 218−226.

(41) Chuang, T. J.; Brundle, C. R.; Rice, D. W. Interpretation of the X-Ray Photoemission Spectra of Cobalt Oxides and Cobalt Oxide Surfaces. *Surf. Sci.* **1976**, *59* (2), 413−429.

(42) Alothman, Z. A. A Review: Fundamental Aspects of Silicate Mesoporous Materials. *Materials* **2012**, *5* (12), 2874−2902.

(43) Luz, G. M.; Mano, J. F. Preparation and Characterization of Bioactive Glass Nanoparticles Prepared by Sol-Gel for Biomedical Applications. *Nanotechnology* **2011**, *22* (49), No. 494014.

(44) Ohtsuki, C.; Kokubo, T.; Yamamuro, T. Mechanism of Apatite Formation on CaO SiO2P2O5 Glasses in a Simulated Body Fluid. *J. Non-Cryst. Solids* **1992**, *143*, 84−92.

(45) Ravarian, R.; Moztarzadeh, F.; Hashjin, M. S.; Rabiee, S. M.; Khoshakhlagh, P.; Tahriri, M. Synthesis, Characterization and Bioactivity Investigation of Bioglass/Hydroxyapatite Composite. *Ceram. Int.* **2010**, *36* (1), 291−297.

(46) Łączka, M.; Cholewa-Kowalska, K.; Osyczka, A. M. Bioactivity and Osteoinductivity of Glasses and Glassceramics and Their Material Determinants. *Ceram. Int.* **2016**, *42* (13), 14313−14325.

(47) Qu, H.; Fu, H.; Han, Z.; Sun, Y. Biomaterials for Bone Tissue Engineering Scaffolds: A Review. *RSC Adv.* **2019**, *9* (45), 26252−26262.

(48) Ghassemi, T.; Shahroodi, A.; Ebrahimzadeh, M. H.; Mousavian, A.; Movaffagh, J.; Moradi, A. Current Concepts in Scaffolding for Bone Tissue Engineering. *Arch. Bone Jt. Surg.* **2018**, *6* (2), 90−99.

(49) Boccardi, E.; Ciraldo, F. E.; Boccaccini, A. R. Bioactive Glass-Ceramic Scaffolds: Processing and Properties. *MRS Bull.* **2017**, *42* (3), 226−232.

(50) Zheng, K.; Fan, Y.; Torre, E.; Balasubramanian, P.; Taccardi, N.; Cassinelli, C.; Morra, M.; Iviglia, G.; Boccaccini, A. R. Incorporation of Boron in Mesoporous Bioactive Glass Nanoparticles Reduces Inflammatory Response and Delays Osteogenic Differentiation. *Part. Part. Syst. Charact.* **2020**, *37* (7), No. 2000054, DOI: 10.1002/ppsc.202000054.

(51) Kurtuldu, F.; Mutlu, N.; Friedrich, R. P.; Beltrán, A. M.; Liverani, L.; Detsch, R.; Alexiou, C.; Galusek, D.; Boccaccini, A. R. Gallium-Containing Mesoporous Nanoparticles Influence in-Vitro Osteogenic and Osteoclastic Activity. *Biomater. Adv.* **2024**, *162*, No. 213922.

(52) Baino, F.; Montazerian, M.; Verné, E. Cobalt-Doped Bioactive Glasses for Biomedical Applications: A Review. *Materials* **2023**, *16* (14), No. 4994.

(53) Ciriminna, R.; Sciortino, M.; Alonzo, G.; De Schrijver, A.; Pagliaro, M. From Molecules to Systems: Sol-Gel Microencapsulation in Silica-Based Materials. *Chem. Rev.* **2011**, *111* (2), 765−789.

(54) Bossard, C.; Granel, H.; Jallot, É.; Montouillout, V.; Fayon, F.; Soulié, J.; Drouet, C.; Wittrant, Y.; Lao, J. Mechanism of Calcium Incorporation Inside Sol-Gel Silicate Bioactive Glass and the Advantage of Using Ca(OH)2 over Other Calcium Sources. *ACS Biomater. Sci. Eng.* **2019**, *5* (11), 5906−5915.

(55) Lin, S.; Ionescu, C.; Pike, K. J.; Smith, M. E.; Jones, J. R. Nanostructure Evolution and Calcium Distribution in Sol-Gel Derived Bioactive Glass. *J. Mater. Chem.* **2009**, *19* (9), 1276−1282.

(56) Zhao, A.; Xiong, B.; Han, Y.; Tong, H. Thermal Decomposition Paths of Calcium Nitrate Tetrahydrate and Calcium Nitrite. *Thermochim. Acta* **2022**, *714*, No. 179264.

(57) Farjadian, F.; Roointan, A.; Mohammadi-Samani, S.; Hosseini, M. Mesoporous Silica Nanoparticles: Synthesis, Pharmaceutical

Applications, Biodistribution, and Biosafety Assessment. *Chem. Eng. J.* **2019**, *359*, 684−705. DOI: 10.1016/j.cej.2018.11.156.

(58) US NTP. Cobalt and Cobalt Compounds That Release Cobalt Ions In Vivo, 2016.

(59) Brauer, D. S. Bioactive Glasses - Structure and Properties. *Angew. Chem., Int. Ed.* **2015**, *54* (14), 4160−4181.

(60) Kargozar, S.; Lotfibakhshaiesh, N.; Ai, J.; Samadikuchaksaraie, A.; Hill, R. G.; Shah, P. A.; Milan, P. B.; Mozafari, M.; Fathi, M.; Joghataei, M. T. Synthesis, Physico-Chemical and Biological Characterization of Strontium and Cobalt Substituted Bioactive Glasses for Bone Tissue Engineering. *J. Non-Cryst. Solids* **2016**, *449*, 133−140.

(61) El-Fiqi, A.; Kim, H. W. Sol-Gel Synthesis and Characterization of Novel Cobalt Ions-Containing Mesoporous Bioactive Glass Nanospheres as Hypoxia and Ferroptosis-Inducing Nanotherapeutics. *J. Non-Cryst. Solids* **2021**, *569*, No. 120999.

(62) Solanki, A. K.; Lali, F. V.; Autefage, H.; Agarwal, S.; Nommeots-Nomm, A.; Metcalfe, A. D.; Stevens, M. M.; Jones, J. R. Bioactive Glasses and Electrospun Composites That Release Cobalt to Stimulate the HIF Pathway for Wound Healing Applications. *Biomater. Res.* **2021**, *25* (1), 1.

(63) Nawaz, Q.; Rehman, M. A. U.; Burkovski, A.; Schmidt, J.; Beltrán, A. M.; Shahid, A.; Alber, N. K.; Peukert, W.; Boccaccini, A. R. Synthesis and Characterization of Manganese Containing Mesoporous Bioactive Glass Nanoparticles for Biomedical Applications. *J. Mater. Sci. Mater. Med.* **2018**, *29* (5), No. 64, DOI: 10.1007/s10856-018-6070-4.

(64) Manzanares, D.; Ceña, V. Endocytosis: The Nanoparticle and Submicron Nanocompounds Gateway into the Cell. *Pharmaceutics* **2020**, *12* (4), 371.

(65) Wei, C.; Wang, X.; Zheng, M.; Cheng, H. Calcium Gradients Underlying Cell Migration. *Curr. Opin. Cell Biol.* **2012**, *24* (2), 254−261.

(66) Petersen, O. H.; Tepikin, A.; Park, M. K. The Endoplasmic Reticulum: One Continuous or Several Separate Ca2+ Stores? *Trends Neurosci.* **2001**, *24* (5), 271−276.

(67) Mitchell, P.; Moyle, J. Chemiosmotic hypothesis of oxidative phosphorylation. *Nature* **1967**, *216*, 615−616.

(68) Maechler, P.; Wollheim, C. B. Mitochondrial Signals in Glucose-Stimulated Insulin Secretion in the Beta Cell. *J. Physiol.* **2000**, *529* (1), 49−56.

(69) Ciftci, E.; Köse, S.; Korkusuz, P.; Timuçin, M.; Korkusuz, F. Boron Containing Nano Hydroxy Apatites (B-N-HAp) Stimulate Mesenchymal Stem Cell Adhesion, Proliferation and Differentiation. *Key Eng. Mater.* **2014**, *631*, 373−378.

(70) Ying, X.; Cheng, S.; Wang, W.; Lin, Z.; Chen, Q.; Zhang, W.; Kou, D.; Shen, Y.; Cheng, X.; Rompis, F. A.; Peng, L.; Lu, C. Z. Effect of Boron on Osteogenic Differentiation of Human Bone Marrow Stromal Cells. *Biol. Trace Elem. Res.* **2011**, *144* (1−3), 306−315.

(71) Wu, C.; Zhou, Y.; Fan, W.; Han, P.; Chang, J.; Yuen, J.; Zhang, M.; Xiao, Y. Hypoxia-Mimicking Mesoporous Bioactive Glass Scaffolds with Controllable Cobalt Ion Release for Bone Tissue Engineering. *Biomaterials* **2012**, *33* (7), 2076−2085.

(72) Ferrol, N.; Donaire, J. P. Effect of Boron on Plasma Membrane Proton Extrusion and Redox Activity in Sunflower Cells. *Plant Sci.* **1992**, *86* (1), 41−47.

(73) Cakmak, I.; Römheld, V. Boron Deficiency-Induced Impairments of Cellular Functions in Plants. *Plant Soil* **1997**, *193* (1−2), 71−83.

(74) Dai, Z. J.; Gao, J.; Ma, X.; Yan, K.; Liu, X. X.; Kang, H. F.; Ji, Z. Z.; Guan, H. T.; Wang, X. J. Up-Regulation of Hypoxia Inducible Factor-1α by Cobalt Chloride Correlates with Proliferation and Apoptosis in PC-2 Cells. *J. Exp. Clin. Cancer Res.* **2012**, *31* (1), 28.

(75) Bosch-Rué, E.; Díez-Tercero, L.; Rodríguez-Gonzá lez, R.; Bosch-Canals, B. M.; Perez, R. A. Assessing the Potential Role of Copper and Cobalt in Stimulating Angiogenesis for Tissue Regeneration. *PLoS One* **2021**, *16* (10), No. e0259125.

(76) Johnson, K. E.; Wilgus, T. A. Vascular Endothelial Growth Factor and Angiogenesis in the Regulation of Cutaneous Wound Repair. *Adv. Wound Care* **2014**, *3* (10), 647−661.

(77) Ateeq, M.; Broadwin, M.; Sellke, F. W.; Abid, M. R. Extracellular Vesicles' Role in Angiogenesis and Altering Angiogenic Signaling. *Med. Sci.* **2024**, *12*, No. 4.

(78) Shibuya, M. Vascular Endothelial Growth Factor and Its Receptor System: Physiological Functions in Angiogenesis and Pathological Roles in Various Diseases. *J. Biochem.* **2013**, *153* (1), 13−19.

(79) Amadio, M.; Govoni, S.; Pascale, A. Targeting VEGF in Eye Neovascularization: What's New?: A Comprehensive Review on Current Therapies and Oligonucleotide-Based Interventions under Development. *Pharmacol. Res.* **2016**, *103*, 253−269.

(80) Shim, J. W.; Madsen, J. R. VEGF Signaling in Neurological Disorders. *Int. J. Mol. Sci.* **2018**, *19* (1), 275.

(81) Penn, J. S.; Madan, A.; Caldwell, R. B.; Bartoli, M.; Caldwell, R. W.; Hartnett, M. E. Vascular Endothelial Growth Factor in Eye Disease. *Prog. Retin. Eye Res.* **2008**, *27* (4), 331−371.

(82) Verheul, H. M.; Pinedo, H. M. The Role of Vascular Endothelial Growth Factor (VEGF) in Tumor Angiogenesis and Early Clinical Development of VEGF-Receptor Kinase Inhibitors. *Clin. Breast Cancer* **2000**, *1*, S80−S84.